LAWRENCE
LIVERMORE
NATIONAL
LABORATORY

UCRL-JRNL-201011

Direct Observations of Phase Transitions in Ti-6Al-4V Alloy Transient Welds using Time Resolved X-Ray Diffraction

J. W. Elmer, T. A. Palmer, S. S Babu, W. Zhang, T. Debroy

November 18, 2003

Journal of Applied Physics

Disclaimer

Direct Observations of Phase Transitions in Ti-6Al-4V Alloy Transient Welds using Time Resolved X-Ray Diffraction

by:

J. W. Elmer[1], T. A. Palmer[1], S. S. Babu[2], W. Zhang[3] and T. DebRoy[3]

[1] Lawrence Livermore National Laboratory, Livermore, CA, 94551, USA
[2] Oak Ridge National Laboratory, Oak Ridge, TN, 37831, USA
[3] The Pennsylvania State University, University Park, PA, 16802, USA

Abstract

Time Resolved X-Ray Diffraction (TRXRD) experiments were used to directly observe phase transformations occurring during gas tungsten arc spot welding of Ti-6Al-4V. These in-situ x-ray diffraction experiments tracked the evolution of the $\alpha \rightarrow \beta \rightarrow L \rightarrow \beta \rightarrow \alpha/\alpha'$ phase transformation sequence in real time during rapid weld heating and cooling. Three different weld locations were examined, providing kinetic information about phase transformations in the fusion zone (FZ) and heat affected zone (HAZ) under different heating and cooling rates and at different temperatures. The TRXRD data were further coupled with the results of thermodynamic calculations of phase equilibria and numerical modeling to compute the weld temperatures. The results suggest that significant superheat is required above the β transus temperature to complete the $\alpha \rightarrow \beta$ transformation at all locations during weld heating, and that the amount of superheat decreases with distance from the center of the weld where the heating rates are lower. Johnson-Mehl-Avrami modeling of the weld heating kinetics produced a set of parameters that allowed the prediction of the $\alpha \rightarrow \beta$ phase transformation rate at each location, but were not successful in determining a definitive mechanism for the

PACS code 64.70.Kb

transformation. The $\beta \rightarrow \alpha$ transformation during weld cooling in the HAZ was shown to initiate at the β transus temperature and reach completion below the Ms temperature, producing substantial α' martensite. In the FZ, the $\beta \rightarrow \alpha$ transformation during weld cooling was shown to initiate below the Ms temperature, and to completely transform the microstructure to α' martensite.

Introduction

Ti-6Al-4V is one of the most commonly used titanium alloys due to its favorable combination of physical and mechanical properties [1-3]. This alloy is oftentimes thermo-mechanically treated to produce a desired amount of equiaxed α and intergranular β with a fine grain size for optimum mechanical properties. However, microstructural changes such as annealing, recrystallization, and phase transformation to high temperature β during welding alter the grain size, phase ratios, and microstructural morphologies in the weld region [4]. The degree to which the microstructure is altered depends on the weld thermal cycles experienced at a particular location, and the kinetics of the various phase transformations taking place here. Although the weld thermal cycles can be calculated with a high degree of confidence using existing numerical models, the same is not true for the phase transformation kinetics under actual welding conditions.

The high heating and cooling rates characteristic of welds require the use of non-conventional methods to study the resulting phase transformations. Time Resolved X-Ray Diffraction (TRXRD) is a method that can be used for real time observations of microstructural evolution taking place under actual welding conditions. In this study, the rapid sampling rate of the TRXRD method was used to investigate the phase

transformations occurring in transient spot welds in Ti-6Al-4V. The fusion zone (FZ), and two different locations in the heat affected zone (HAZ) of the weld were examined. At these different locations, the $\alpha \rightarrow \beta$ transformation proceeds under different heating rates to different peak temperatures, resulting in different microstructures at each location prior to cooling.

Computational thermal fluids modeling and computational thermodynamics were used to calculate weld temperatures and key phase transformation temperatures. By combining computed temperatures and the TRXRD data, kinetics of the phase transformations in Ti-6Al-4V were determined. Of particular interest were the mechanisms for the $\alpha \rightarrow \beta$ transformation on heating and the $\beta \rightarrow \alpha$ transformation on cooling, and the role of nucleation in these welding induced transformations. The results of this investigation show that a significant amount of superheating is required to transform the microstructure on weld heating. Furthermore, martensite was shown to occur during cooling, and its formation was influenced by the FZ and HAZ microstructure at the initiation of the cooling cycle.

Experimental Procedures

Materials and Welding

Ti-6Al-4V ELI (extra low interstitial) was acquired in a 114 mm diameter bar. Samples were machined from the bar in preparation for the TRXRD experiments that measured 100 mm in diameter and 75 mm in length. Chemical analysis was performed on the starting material to give its composition as follows (by wt. percent): 6.0 Al, 4.2 V, 0.11 O, 0.17 Fe, 0.0028 H, 0.014 C, 0.009 N, 0.03 Si, bal. Ti. Figure 1 shows the

microstructure of the starting material, which contains approximately 12% β distributed intergranularly around the slightly elongated α grains that form the matrix. The α grains of the starting material have an aspect ratio of approximately 2:1, with an average grain size of 5.8 μm across the small dimension of the grains.

Gas tungsten arc spot welds were made on the Ti-6Al-4V alloy bars by striking a stationary arc, maintaining this arc for a fixed amount of time, then extinguishing the arc to let the weld cool. TRXRD data were gathered over a period of 60 s during welding, allowing both the heating and cooling cycles to be observed during one weld. Three different experimental conditions were investigated by positioning the x-ray beam at three locations. At the first location (4.5 mm from the weld center), the temperature-time profile of the weld was sufficient to melt and resolidify the alloy. At the second location (5.0 mm from the weld center) the time temperature profile was sufficient to completely transform the alloy to the high temperature β phase during heating. At the third location (5.5 mm from the weld center) the time-temperature profile was only capable of producing a partial transformation to the β phase during heating. The welding parameters used in this study were 100 amps at 19 volts with an arc on time of 17s to 20s, and produced weld pools with a diameters just less than 10 mm. Additional details about the welding parameters are summarized in Table 1.

All of the welds were made inside an environmentally controlled chamber that was backfilled with high purity helium to deliver the x-ray beam with minimal attenuation, and to prevent oxidation of the titanium alloy surface that would otherwise occur during welding. In addition, a cross jet of helium gas was directed at the x-ray beam impingement location to prevent metal vapors from depositing on the surface where

x-ray diffraction was taking place. After the TRXRD experiments were completed, metallographic inspection was performed by sectioning and polishing the welds using standard metallographic procedures. The samples were then chemically etched using either a solution containing 5 ml HF, 10 mL HNO_3, 30 mL lactic acid for approximately 30s to reveal the base metal and weld microstructures. Remmington B etchant (10 ml HF, 10 ml glycol for approximately 1 minute) was used to reveal the fusion zone boundary.

Microchemical compositions of the starting α and β phases were determined using microprobe analysis. The data were collected on a JEOL-8200 microprobe, operating at 15 KV and a beam current of 20 nA. Individual point locations were inspected using a beam diameter of 1 μm, while "broad beam" analysis was obtained by rastering a 1μm beam over a 100 μm x 100 μm raster. X-ray intensities were calibrated using Ti, V, Al, Fe and SiO_2 for oxygen, and corrected to wt% using the ZAF corrections. The intensities were also run using TiO_2 and Al_2O_3 as standards and yielded result within error of those calibrated using Ti and Al. Results of the microchemical analysis of each phase in the starting material are shown in Table 2. These compositions represent the average of seven locations for each phase, and the estimated error corresponds to a one σ variation about the mean. It is clear from these results that V and Fe partition to the β phase, while Al partitions to the α phase. In addition to the microchemical composition information, backscattered electron images taken of the polished surface were used to show the initial area fraction of β in the microstructure to be 12.1%.

Time Resolved X-Ray Diffraction.

TRXRD measurements were performed on a 31-pole wiggler beamline (10-2) at the Stanford Synchroton Radiation Laboratory (SSRL) with SPEAR (Stanford Positron Electron Accumulation Ring) operating at an electron energy of 3.0 GeV and an injection current of ~100 mA [5]. Details of similar welding experiments have been previously published for commercially pure titanium [6-10], C-Mn steels [11-13] and stainless steels [14,15]. Figure 2 shows a schematic drawing of the experimental setup where the focused synchrotron beam is passed through a monochromator before passing through a 540 μm diameter tungsten pinhole. This setup renders a ~600μm diameter monochromatic beam on the sample at an incident angle of ~25°. The beam flux was measured to be ~10^{12} photons/s as measured by an ion gage detector placed immediately downstream from the 540 μm pinhole. The photon energy used for all the experiments was 12.0 keV (λ = 0.1033 nm).

One difference between the experiments presented here and those performed in the past is the intensity of the x-ray beam, which is nearly 2 orders of magnitude greater than before. This higher flux is the result of the recent installation of a liquid nitrogen cooled monochronometer and a new x-ray focusing mirror on the beam-line. This increased flux provides higher quality diffraction peaks for a given pinhole size and counting time, enhancing peak profile analysis for more accurate measurements of the 2θ peak positions and peak shape determination.

In the TRXRD experiments, the x-ray beam is positioned a fixed distance from the electrode. At this location, 600 diffraction patterns are collected at a 0.1s/pattern

interval during welding. The diffraction patterns were recorded using a 50 mm long 2048 element position sensitive Si photodiode array detector. This detector was placed ~100 mm behind the weld to cover a 2θ range from 22° to 52°. At 12.0 keV, this 2θ range covers three possible β-titanium peaks: bcc (110), bcc (200), and bcc(211); and 9 possible α-titanium (hcp) peaks. Figure 3 shows the ideal (powder pattern) calculated positions of the peaks in both phases at room temperature [16], using lattice constants of a=0.33065 nm for β (bcc), and a= 0.29506 nm, c=0.46788 nm for α (hcp) [17], and compares these peaks with the 2θ range covered by the x-ray detector. In this diffraction pattern, the peak positions and intensities of pure titanium at room temperature, and each phase is assumed to represented in roughly equal volume fractions. In the actual material alloying elements, as expected, alter the peak positions and the phase ratios from the calculated values.

Figure 4 shows one of the TRXRD patterns taken directly on the Ti-6Al-4V bar prior to welding. Since the alloy contains approximately 88% α at room temperature, the diffraction pattern is dominated by the hcp α diffraction peaks. All nine hcp peaks are present, in slightly different proportions to those calculated for powder diffraction due to texture in the starting material. The small amount of β phase in the starting microstructure diminishes the intensity of the β diffraction peaks, and only two of these peaks, bcc(110) and bcc(200), can be distinguished in the diffraction pattern at room temperature. The positions of the observed peaks have shifted from those calculated for pure titanium. For example, the bcc(110) has shifted to higher 2θ values relative to the hcp(002), and now appears directly between the hcp(002) and hcp(101) peaks at room temperature.

Results

Phase Equilibria

In Ti-6V-4Al, V stabilizes the bcc crystal structure of the β phase, while Al stabilizes the hcp crystal structure of the α phase. Two calculated pseudobinary diagrams for this alloy are shown in Fig 5; one illustrating the influence of V on the α/β binary alloy equilibria, and the other illustrating the influence of Al on the α/β binary alloy equilibria. These calculations were performed using ThermoCalc[18] with the Ti-Data data base (Distributed by UES Software), by considering the influence of Ti, V, Al, Fe and O on phase equilibria at the nominal alloy composition.

The phase relationships presented in Fig. 5 indicate that the amount of β phase will increase during heating, completely transforming to β at a temperature of 956°C. Above this temperature, the β phase is stable up to the solidus temperature of 1693°C, while complete melting occurs at the liquidus temperature of 1701°C. These temperatures are slightly different than those published elsewhere based on experimental measurements [2], where the liquidus is reported to be 1655°C, the solidus to be 1605°C, and the β transus to be 975°C. In the results that follow, the experimentally determined values will be used here to represent the phase transformation temperatures, and Thermocalc to illustrate compositional effects on phase stability.

The relatively large difference in liquidus and β-transus temperature suggests that the liquid weld pool should be surrounded by a relatively large region of β that varies in size in response to varying temperature gradients around the weld pool. Outside of this single phase β region, the α phase would be expected to coexist with β in varying amounts during welding, thus providing a transition to the reduced amount of β in the

base metal. Since equilibrium is rarely attained during welding, the microstructures that form are often considerably different than those expected from the calculated phase diagram. Furthermore, the evolution of weld microstructures can be difficult to determine in titanium alloys using conventional techniques since the microstructures that form during heating are subsequently altered by the subsequent solid state transformations that take place during cooling.

Weld Microstructure

Figure 6a shows a cross section of one of the spot welded samples to demonstrate the complexity of the Ti-6Al-4V weld microstructures. The fusion zone (FZ) is characterized by the appearance of large columnar grains that solidified as β and subsequently underwent a near complete transition to a finely dispersed α or α′ phase. The α′ phase is a martensitic phase with an hcp crystal structure and similar lattice parameters to the α phase [2]. The FZ grains grew from the large β grains of the HAZ where it is often difficult to distinguish the FZ and HAZ grains from each other. In this microstructure the HAZ/FZ boundary was revealed, using careful metallographic preparation techniques, as a dark etching line running through the columnar grains. This boundary is identified by the arrows in Fig. 6a. It is clear that solidification occurred by epitaxial regrowth from the large HAZ grains. Outside the fusion zone, there is a gradient of prior β grain sizes extending from the HAZ/FZ boundary to the region of α/β coexistence. The region of co-existence extends outward along the heat flow direction, reaching the unaffected base metal in the clearly defined semi-circular cross sectional boundary that measures approximately 6 mm from the center of the weld. This post-weld

characterization is useful in illustrating the final weld microstructure. However, it is not possible to reveal any information about the phase transition kinetics from the post-weld microstructure alone.

Time Resolved X-Ray Diffraction

The locations where the TRXRD measurements were taken are shown in Fig. 6b. Each TRXRD data set consisted of a series of 600 diffraction patterns taken at 100 ms intervals. This large amount of data is difficult to visualize in detail, however it can be reproduced in different formats to illustrate the sequence of phase transformation events that take place during welding. One method to represent the data is to plot the data as a pseudo-color image, where the intensity of the color represents the intensity of the diffraction peaks.

Figure 7 plots the pseudo-color TRXRD data set for weld 1 which underwent melting and solidification. The 2θ locations of the peaks are plotted along the x-axis, and weld time on the y-axis. The seven prominent peaks at the beginning of the weld are all indexed to the α phase. The β peaks, although present, have too low of an intensity to be visible in this pseudo-color overview at the beginning of the weld. After the arc is initiated at t=5.8s (note faint horizontal line caused when the arc was struck), these peaks move towards lower 2θ values due to thermal expansion. The α peaks decrease to zero intensity at t=17.8s, leaving the three β peaks as indicated by the arrows. The intensity of the β peaks then decreases to zero as the alloy melts at t=23.8s. The arc is extinguished at t=25s (note faint horizontal line caused by the arc termination). Almost immediately the β phase appears, indicating β solidification from the melt. The β peaks only exist for

a short time, and rapidly shift to higher 2θ values, indicating the cooling effect on the lattice parameter. Transformation to the α phase occurs rapidly, where eight prominent diffraction peaks from the α phase remain for the remainder of the experiment.

The TRXRD results of the other two experiments duplicate similar phase transformation progressions to that shown in Fig. 7. However, no melting was observed in these welds. In weld 2, the complete transformation to β was observed, and was accompanied by the complete disappearance of the hcp diffraction peaks. In weld 3 only partial transformation to β was observed, so both bcc and hcp diffraction peaks were present throughout the entire TRXRD run.

Analysis of every peak in each of the diffraction patterns was performed to estimate the relative fraction of the hcp and bcc titanium phases present as a function of weld time. To do this, the integrated intensity of each peak in each diffraction pattern was measured using a sum of one or more Gaussian peak profile fitting functions [8, 15]. The area and FWHM values of the fitted peaks were then determined using an automated curve-fitting routine developed in Igor Pro®, Version 4.0 [19].

Using the TRXRD measured areas of the x-ray diffraction peaks, the area fraction of the β peaks was calculated as the total area of the β peaks divided by the combined areas of the β and α peaks. Then, using the metallographically measured amount of β phase in the starting microstructure (12.1%) for calibration, the x-ray diffraction measurements of the β peak areas were converted into actual amount of the β phase throughout the TRXRD run. The fraction α was further calculated by subtracting the fraction β from unity, since only these two phases are present in the microstructure.

Each TRXRD run was analyzed using the integrated peak intensities to determine the fraction of the β phase as a function of weld time. Figure 8 plots this result for weld 1, which underwent melting and solidification. In this plot, the time scale is set equal to zero at the point of arc initiation. The fraction of the β phase at this location remains at or about its base metal value for approximately 6s, then begins to increase, and completely transforms to the β phase at t=13.5 s. One second later, the β phase begins to melt and the sample is completely molten by t=15.7s. Solidification to the single phase β begins rapidly after the arc is extinguished. The β phase is then stable for 0.9s before the first appearance of α on cooling, and rapidly transforms to α/α´ as the weld cools. The fraction β reaches its base metal value 1.9s after the first α peaks were observed on cooling. Therefore, at this location, the complete $\alpha \rightarrow \beta \rightarrow L \rightarrow \beta \rightarrow \alpha/\alpha'$ transformation sequence was observed during welding, and the changes in crystal structure were recorded with a time resolution of 0.1s.

Similar plots are presented in Fig. 9 and Fig. 10 for the two HAZ weld locations. Figure 9 plots the β fraction versus time for weld 2, which underwent a complete transformation to β, but did not reach high enough temperatures to melt. The overall trend of increasing fraction of β with time is similar to that in weld 1. However, the complete transformation to β occurred later, requiring 16.7s after arc initiation as compared to 13.5s for weld 1. On cooling, the reverse transformation from β to its base metal required 4.2s for this weld, which is longer than that of weld 1 which required only 1.9s to take place. At the weld 3 location, which is shown in Fig. 10, the peak temperature was not high enough to completely transform the microstructure to β. The

initial increase in β begins at t=9s, which is approximately 1s later than that of weld 2, and 2s later than that of weld 1.

Coupled Thermal-Fluids Numerical Modeling

Whereas the TRXRD results presented in Figs 8-10 show changes in the fraction β phase as a function of time, these data only provide limited information about the transformation kinetics since weld temperature has not yet been incorporated into the plot. In order to relate weld time to weld temperature, we use numerical modeling since transient weld temperatures are extremely difficult to measure directly. The weld model used here is a well tested 3D numerical heat transfer and fluid flow model as described in detail in reference [20] for a flat plate geometry. No significant error was introduced due to the heat transfer calculations in the flat geometry since the weld pool dimensions were much smaller than the dimensions of the cylindrical bar. The weld pool boundary, i.e., liquid/solid interface, is traced using an enthalpy-porosity technique in a fixed Cartesian coordinate system [20]. The calculations take into account the electromagnetic, surface tension gradient and buoyancy driving forces present in the transient weld pool convection, and also consider a variable arc efficiency for the first 2s of arc on time as the arc establishes itself. In addition, at the weld top surface, the heat loss due to the helium shielding gas is considered by using Newton's law of cooling with an appropriate heat transfer coefficient, as summarized in the appendix.

For computational accuracy, a very fine grid system consisting of 110×55×48 grid points was used, and the corresponding computational domain had dimensions of 92 mm long, 46 mm wide and 32 mm deep. Spatially non-uniform grids were used for

maximum resolution of the variables, such that the grid spacing was refined near the heat source where the temperature gradients are the highest. The minimum grid spacing along the x and z directions were about 100 μm and 10 μm, respectively. Small time steps of 0.1 s were further required to track the weld pool size and shape under the high heating and cooling rates produced under the transient welding conditions [20].

The thermophysical properties used to represent the Ti-6Al-4V alloy in the calculations are given in Table 1 [21, 22]. It should be noted that the specific heat (C_P), thermal conductivity (k) and density (ρ) of Ti-6Al-4V vary with temperature [21]. Hence, accurate calculations of weld temperature need to consider the temperature dependence of these properties. However, if the C_P, k and ρ are all taken as temperature dependent, the computational task is very difficult. Therefore, in the present calculations, only k is treated as temperature dependent, while C_P and ρ are assumed to be constant. This approach largely simplifies the model, while still preserving significant accuracy since these thermophysical properties are of importance in their combined form, i.e., $k / (\rho C_P)$. For the Ti-6Al-4V alloy, the thermal conductivity of solid increases from 8.3 W/m-K at 300 K to 24.2 W/m-K at 1900 K.

The cross sectional shape of the calculated weld pool at its maximum size matched the experimental weld cross section having a width just under 10 mm and a maximum depth of 1.3 mm. Using the results from the weld model, the temperature distributions, heating rates, and cooling rates are calculated as a function of welding time at each TRXRD location. The calculated weld time-temperature plots for each of the three x-ray locations are shown in Fig. 11, and are compared to the calculated liquidus temperature of the Ti-6Al-4V alloy. It is clear that the monitoring location closest to the

center of the weld heated the fastest, and is the only location of the three to reach the liquidus temperature. The other two x-ray locations have temperatures that exceed the β transus temperature and are held above this temperature for times in excess of 10 s prior to extinguishing the arc. In this figure, the solid circles mark the times where the TRXRD measurements showed that the transformation to β was complete, the triangle where melting began, and the square where melting was complete.

Discussion

The calculated α/β phase equilibria indicated that the fraction of the β phase will reach unity at a the β transus temperature. This relationship can be explored more closely by using the thermodynamic software to calculate the equilibrium volume fraction of β as a function of temperature. These results are plotted in Fig. 12, which shows that the fraction of β is relatively constant, at about 4%, up to a temperature of approximately 450 ºC. In fact, the calculations predict a slight dip in the fraction of β, due to the retrograde in the α phase field as shown in Fig. 5. Above 450 ºC, the β fraction increases at an increasing rate, until complete transformation occurs at the β transus.

The calculated β fraction, which is plotted versus temperature in Fig.12, has a similar shape to that of the heating stages of the TRXRD measurements shown in Figs 8-10. In these figures, the β content is relatively low and constant during the initial heating stages, but then rapidly increases at higher temperatures. However, the non-uniform weld heating rate, indicated in Fig. 11, needs to be considered in order to better compare the TRXRD measurements with the thermodynamic predictions.

The weld temperature not only influences the α/β phase ratio, but also the individual compositions of the α and β phases. Variations in the composition of these phases are predicted with thermodynamic calculations, as illustrated in Fig. 13. These results show that the composition of the α phase changes very little over the entire temperature range up to the β transus temperature. However, the β phase shows a dramatic variation in composition, whereby V concentrates strongly during cooling. The reason for this behavior is related to the solubility of V in the α phase, which is small and relatively constant. Therefore, as the alloy transforms from $\beta \rightarrow \alpha$ as the temperature decreases, the V concentration in β increases dramatically to accommodate nearly all of the V into the smaller and smaller volume fraction of the remaining β.

Transformation kinetics during weld heating

The fraction of β versus weld temperature can be determined by combining the calculated thermal profiles with the TRXRD integrated peak area analyses. This correlation was performed and the results are illustrated in Figs 14a-b, which replots the fraction of β measured in the TRXRD experiments as a function of weld time and weld temperature respectively. In these figures, the data for the three TRXRD locations are represented by the symbols, and kinetic modeling results are shown by the solid lines. The modeling results are discussed in more detail later. The data plotted versus weld time in Fig. 14a show that the transformation follows a general sigmoidal shape curve at each location. More rapid heating and higher transformation rates occur at the locations closest to the center of the weld, when the microstructure is completely transformed to β.

Figure 14b shows this same data plotted versus temperature. Here, the location farthest from the center of the weld begins to transform at a lower temperature than the other two locations. Still a significant superheat above the β transus is required before transformation is first observed. The fact that the location furthest from the weld center begins to transform at lower temperatures, is related to the time-temperature kinetics of the $\alpha \rightarrow \beta$ phase transformation. Higher amounts of superheat are required at locations closer to the weld center where the heating rates are higher.

The kinetics of the $\alpha \rightarrow \beta$ phase transformation at each location were modeled using the Johnson-Mehl-Avrami (JMA) approach to develop a set of parameters that could be used to predict the extent of the phase transformation for different weld heating rates. The JMA approach is represented by the following expression [23]:

$$f_e(t) = 1 - \exp\{-(kt)^n\} \qquad (1)$$

where $f_e(t)$ is the extent of the transformation at a given time t, n is the JMA exponent, and k is a rate constant given as:

$$k = k_0 \exp(-\frac{Q}{RT}) \qquad (2)$$

where k_0 is a pre-exponential constant, Q is the activation energy of the transformation including the driving forces for both nucleation and growth, R is the gas constant, and T is the absolute temperature.

Although the activation energy of phase transformations occurring under isothermal conditions is often known, the overall activation energy under non-isothermal welding conditions is rarely known when nucleation and growth are simultaneously operating. This is because the contributions of nucleation to the overall activation energy

are temperature and rate dependent [24], and are further influenced by the starting microstructure [23]. Thus, a unique activation energy for the overall transformation is not always possible to determine. However, if a given transformation has a large growth component, it may be treated as a growth controlled mechanism, and the activation energy for growth provides a reasonable starting assumption.

Equations 1 and 2 were discretized and numerically integrated over the non-isothermal heating profile of the weld following a previously developed procedure whereby transformation in a two-phase field can be taken into account [12]. To do this, the TRXRD data were fit using the JMA parameters (n, ko, and Q), by selecting one of the JMA parameters and calculating the remaining two using a numerical data fitting procedure [12].

In the first calculation, the activation energy for the diffusion of V is used to represent a growth controlled phase transformation mechanism where nucleation is assumed to not play a significant role [24]. Since the V content of the α phase is nearly constant up to the β transus temperature, V diffusion in α will not be a rate controlling factor. Instead, the transport of V through the β phase will control the transformation rate, assuming the interface mobility of the α/β interface is high [24]. The diffusion coefficient for V in the β phase can be represented by an Arhennius expression, $D = A \exp(-Q/RT)$, and has been measured to have an activation energy Q=123.9 kJ/mole, with a pre-exponential of $A=1.6\times10^{-4}$ cm^2s^{-1} for a binary Ti-V alloy containing 10 a/oV [22].

The optimum JMA parameters (n and ko) for the diffusion controlled growth assumption with an activation energy of Q=123.9 kJ/mole were calculated by minimizing the error between the JMA fit and the TRXRD data at each weld location. The results are

summarized in Table 4, showing that the average error between the fit and the data points is small for all cases. The calculated ln(ko) values varied between 5.8 and 6.4. The n values varied from 6.3 to 10.5. Even though the JMA fit to the data is good in all cases, the calculated n values are higher than expected for a diffusion controlled growth transformation, where a value of n=4.0 would be considered to be representative [23].

The calculations were then performed using a different set of assumptions where nucleation and growth would simultaneously occur. This time, a reasonable value of n=4 was selected for a transformation mechanism that involves a strong nucleation component [23]. Using this assumption, ko and Q were calculated using the same JMA modeling approach. The reasoning here is that although the activation energy for growth is temperature independent the activation energy for nucleation is temperature dependant [25], and therefore the combination of the two may result in an activation energy different than either one alone. The results of these calculations are also summarized in Table 4, showing again that the average error between the fit and the data points is small for all cases, and better than the previous fits where Q was held constant. This time the ln(ko) values varied between 8.2 and 12.0, increasing with distance from the center of the weld. The calculated activation energy for the transformation varied from 144 to 188 kJ/mole, increasing with distance from the center of the weld. The results of these calculations are superimposed as the solid lines over the measured fraction of β versus time and temperature plots shown in Fig. 14b, illustrating the good data fit in all three cases.

The range in JMA parameters for the three data sets is reasonably small, suggesting that the same phase transformation mechanism may be operating at each

location. Therefore, it is possible to optimize all of the data sets together to produce one set of JMA parameters to represent the transformation. The results of this calculation are also summarized in Table 4 for both the n=4 assumption and the Q=123.9 kJ/mole assumption. The fit to the data is better for the n=4 assumption, which results in an overall activation energy Q=189 kJ/mole and a corresponding value of ln(ko)=11.4.

To summarize the results of the JMA calculations, two different starting assumptions led to different values for the activation energy for the transformation. The difficulties associated with using the JMA approach to determine activation energies for transformations involving nucleation and growth have been observed by other investigators [26], and additional studies will be required to provide more conclusive evidence for the transformation mechanism during transient weld heating of Ti-6Al-4V. However, the JMA modeling approach did successfully produce sets of parameters (Q=189kJ/mole, n=4.0 and ln(ko)=11.4) that allow the weld heating transformation rate to be predicted, even though the transformation mechanism was not definitively established.

Transformation kinetics during weld cooling

Once the arc is extinguished, the weld cools rapidly and β begins to transform to α/α´. The β→α transformation on cooling have several differences from the α→β transformation on heating. The temperature profiles plotted in Fig. 11 show that the heating rates at the β transus temperature vary from 120 to 360 ºC/s, whereas the cooling rates vary from 1430 ºC/s to 2000 ºC/s at the time the arc is terminated to 530 ºC/s at the β transus temperature.

The second difference relates to the nature of the microstructures at each of the three weld locations. Weld 1, closest to the center of the weld, undergoes melting and solidification to β prior to beginning the β→α transformation on cooling. Thus the microstructure is composed entirely of large columnar β grains that formed during solidification, and would require nucleation of the α phase before transformation can begin. Weld 2, in the hottest portion of the HAZ, underwent a complete transformation to β and experienced grain growth at these elevated temperatures. The resulting microstructure is therefore also composed entirely of large β grains and would require nucleation of the α phase before transformation can begin. However, the nucleation conditions would most likely be different at these locations because the grain growth and chemical homogenization that occurs in the HAZ is different than what occurs during solidification. Weld 3, the furthest from the center of the weld, never transformed completely to β, and therefore contains a mixture of α and β at the time when the reverse transformation to α begins. Therefore this location would not require nucleation of α prior to the β→α transformation. Thus the difference in microstructures, combined with the high cooling rates, should lead to different transformation kinetics on cooling than on heating.

The results of the TRXRD measurements showing the fraction of β during weld cooling time are plotted in Fig. 15a, where time equal to zero represents the time when the arc was extinguished. In this figure, the amount of β versus cooling time is plotted for each of the three locations. At the location furthest from the weld center, the amount of β shows an overall increase after the arc is extinguished. This behavior is the result of the incomplete transformation to β and the fact that the temperature is still above the β

transus for some time after the arc is turned off. Thus, even though the weld is cooling, the $\alpha \rightarrow \beta$ transformation continues for approximately 0.5 s. The transformation to α then commences, and the β content decreases nearly to zero, approximately 4s after the arc has been extinguished. Weld 2, in the HAZ adjacent to the fusion boundary, maintains 100% β for nearly 1s after the arc has been extinguished, before beginning to transform to α. Nearly complete transformation to α occurs at this location approximately 3s after the arc was extinguished. Weld 1, closest to the center of the weld, is liquid when the arc is extinguished, and continues to be molten for approximately 1s prior to solidifying completely to the β phase. The β is stable for approximately 1s before beginning to transform to α/α'. This transformation reaches completion approximately 3.5s after the arc has been extinguished.

These data are further plotted in Fig. 15b as a function of the calculated weld temperature. This figure shows that the $\beta \rightarrow \alpha$ transformation begins at a different temperature at each location. In the two HAZ locations, the reverse transformation to α/α' occurs at, or very near, the β transus temperature. However, for the weld in the FZ, the transformation is first observed at 600ºC, which corresponds to approximately 375ºC of undercooling below the β transus, and is also below the Ms temperature.

The transformation kinetics at each of location vary significantly, and do so in response to the different microstructures that evolved at these different locations during the heating cycle of the weld. The location showing the most transformation at temperatures close to the β transus is the location furthest from the center of the weld. Since both α and β are present in the microstructure no nucleation is required, and the transformation quickly commences as the temperature falls below the β transus.

The next HAZ region, which is closer to the center of the weld at monitoring location 2, completely transformed to β during heating, and experienced grain growth prior to the back transformation to α during weld cooling. Here, the transformation began at the β transus, but did so very slowly, which may be an indication that nucleation of α was required. Note again that the transformation appears to arrest at a β fraction of approximately 0.9 before commencing again on further cooling.

The location closest to the center of the weld, which was in the FZ, showed significant undercooling prior to beginning the back transformation to α/α´. At this location, which has the largest β grains, the undercooing below the β transus was measured to be 375 ºC before the presence of α/α´ was detected at approximately 3.5s after the β transus was reached. Again an arrest in the transformation was observed at a β fraction of approximately 0.9 before commencing again on further cooling

Qualitatively, the decreasing amounts of transformation at a given temperature at locations closer to the center of the weld are expected from nucleation and growth theory. Quantitatively, this behavior is more difficult to describe due to the multiple changes associated with the different thermal and microstructural histories at each location. Experiments and modeling of the $\beta \rightarrow \alpha$ phase transformation in Ti-6Al-4V have been performed to better understand the individual roles of nucleation and growth at different cooling rates [25]. Katzov et al. showed that the thickness of the α lamella decreased with increasing cooling rate, and the amount of transformation that occurred at a given temperature decreased with increasing cooling rate [25]. These facts were related to the decrease in the temperature where the peak nucleation rate occurs and to the reduced time for the $\beta \rightarrow \alpha$ phase transformation to take place as the cooling rate was increased. Their

work was performed at much lower cooling rates than those experienced by the welds in this investigation, and for a growth controlled transformation to the α phase. However, there is a high likelihood that α′ martensite is forming in the high cooling rate welds produced in this study.

The microstructures of the weld FZ and are shown in Fig. 16 at the three locations representative of where the x-ray diffraction measurements were taken. The microstructures show the presence of α′ martensite with its characteristic needle-shaped morphology [2]. This microstructure forms when untransformed β is subjected to temperatures below the martensite start temperature (Ms) on cooling. The Ms temperature for Ti-6Al-4V is approximately 650ºC [2], but varies with chemical inhomogeniety of the β phase. Although each location contains α′ martensite, the amount and distribution differ at each location. Fig. 16a shows the microstrucure at location 1 in the FZ. At this magnification, the microstructure appears to be composed entirely of α′ martensite, where the length of many of the needles exceeds 100 μm. This microstructure has no obvious signs of retained β, and appears to form entirely through the diffusionless martensitic mechanism. This microstructure is consistent with the TRXRD data and the computed temperatures, showing that all of the transformation occurred below the Ms temperature.

The microstructures at the HAZ locations contain some features not present in the FZ. The microstructure of weld location 2 is shown in Fig. 16b and contains a dark etching phase between some of the α′ martensite needles. This dark etching phase is presumably retained β, and the patches seen in the upper left hand side of the micrograph are on the order of 10 μm. Figure 16c shows the microstructure of weld location 3,

which also contains retained β phase, but in higher amounts than at weld location 2. In places, the elongated patches of retained β reach lengths of nearly 100 μm, while never exceeding 10 μm in thickness. Another difference between this microstructure and the previous microstructures is the length of the α′ martensite needles, which are shorter at this location than at the other locations. The reason for the reduced length of the α′ martensite needles is most likely the presence of α at the time when β began its back transformation on cooling in this partially transformed region of the HAZ. The presence of α in the incompletely transformed microstructure may inhibit growth of α′ martensite needles.

The microstructures presented in Figs 16a-c show a decrease in the martensite content as the distance from the center of the weld increases. The decreasing amount of martensite with distance is consistent with the TRXRD observations, whereby transformations in the FZ took place entirely below the Ms temperature of the alloy. In the HAZ locations, TRXRD showed that the β→α transformation initiated at the β-transus, but completed below the Ms temperature. This is also consistent with the metallographic observations. Additional work needs to be performed to see if the TRXRD transformation curves can be correlated to changes in the transformation mechanisms, and if specific kinetic data can be extracted from these measurements.

Conclusions

1. TRXRD experiments employing synchrotron radiation were performed *in-situ* on transient GTA welds on Ti-6Al-4V alloys, providing real time observations of the $\alpha \rightarrow \beta \rightarrow L \rightarrow \beta \rightarrow \alpha/\alpha'$ phase transformation sequence in both the weld FZ and HAZ.
2. A 3D transient numerical weld model was used to predict weld temperatures as a function of weld time and location. The model calculated the evolution of the FZ velocity fields and temperatures, and was validated by comparing the predicted and experimentally measured geometry of the FZ.
3. During weld heating, the TRXRD measurements showed that the $\alpha \rightarrow \beta$ transformation took place above the β transus temperature with significant superheat required for completion due to the rapid heating rate of the weld. Decreasing amounts of superheat were required at distances further from the weld center due to the corresponding decrease in heating rates.
4. The kinetics of the $\alpha \rightarrow \beta$ transformation on heating were modeled using a modified JMA approach using different assumptions about the mechanisms for nucleation and growth. These results produced a set of JMA parameters for the prediction of the transformation rate (Q=189 kJ/mole, ln(ko)=11.4, n=4.0), but were not successful in determining a definite mechanism for the overall transformation.
5. During weld cooling in the HAZ, TRXRD measurements showed that the $\beta \rightarrow \alpha$ transformation initiated at the β transus temperature, but completed the transformation below the Ms temperature. The transition from $\beta \rightarrow \alpha$ to $\beta \rightarrow \alpha'$ appeared to take place after approximately 5-10% of the microstructure had initially

transformed to α in both the partially transformed and the completely transformed regions of the HAZ.

6. During weld cooling in the FZ, TRXRD measurements showed that the initiation of the $\beta \rightarrow \alpha'$ transformation began at temperatures at or below the Ms temperature. Once initiated, the transformation occurred rapidly and nearly completely to α' martensite in less than 2s over a temperature range of approximately 200ºC.

Acknowledgments

This work was performed under the auspices of the U. S. Department of Energy by UC, Lawrence Livermore National Laboratory, under Contract No. W-7405-ENG-48, and the LLNL portions of this work were supported by DOE, Office of Basic Energy Sciences, Division of Materials Science. Part of the research was sponsored by the U.S. Department of Energy Division of Materials Sciences and Engineering under contract No. DE-AC05-00OR22725 with UT-Battelle, LLC. Portions of this research were also carried out at the Stanford Synchrotron Radiation Laboratory, a national user facility operated by Stanford University on behalf of the U.S. Department of Energy, Office of Basic Energy Sciences. The authors express gratitude to Mr. Bob Vallier of LLNL for performing optical metallography, and Mr. Octavio Cervantes for performing x-ray diffraction simulations using JADE software.

References

1. M. Donachie, Jr.: Titanium A Technical Guide, *ASM International*, 1989.
2. Material Properties Handbook: Titanium Alloys, *ASM International*, 1994.
3. ASM Handbook, Volume 6: Welding, Brazing and Soldering, *ASM International*, 1993.
4. Ø. Grong: Metallurgical Modelling of Welding, *The Institute of Materials*, London, 1994.
5. V. Karpenko, J.H. Kinney, S. Kulkarni, K. Neufeld, C. Poppe, K.G. Tirsell, Joe Wong, J. Cerino, T. Troxel, J. Yang, E. Hoyer, M. Green, D. Humpries, S. Marks, and D. Plate: *Rev. Sci. Instrum.*, 60, pp. 1451-1460, 1989.
6. J. W. Elmer, Joe Wong, M. Fröba, P. A. Waide and E. M. Larson, "Analysis of Heat Affected Zone Phase Transitions Using In-Situ Spatially Resolved X-Ray Diffraction With Synchrotron Radiation," *Metall. Mater. Trans. A*, 27A(3), p. 775, 1996.
7. J. W. Elmer, Joe Wong and Thorsten Ressler, "Spatially Resolved X-Ray Diffraction Phase Mapping and $\alpha \rightarrow \beta \rightarrow \alpha$ Transition Kinetics in the HAZ of Commercially Pure Titanium Arc Welds," *Metall. and Mater. Trans. A*, 29A(11), p. 2761, 1998.
8. J. W. Elmer, T. A. Palmer and Joe Wong, "In-Situ Observations of Phase Transitions in Ti-6Al-4V Alloy Welds using Spatially Resolved X-Ray Diffraction," *Journal of Applied Physics*, V93(4), pp1941-1947, 15 Feb., 2003.
9. Z. Yang, J. W. Elmer, Joe Wong, and T. DebRoy, "Evolution of Titanium Arc Weldment Macro- and Microstructures – Modeling and Real Time Mapping of Phases," *Welding Journal*, 79(4), p. 97s-112s, 2000.
10. Joe Wong, M. Fröba, J. W. Elmer, and P. A. Waide "In-Situ Phase Mapping and Transition Study in Fusion Welds," *J. Mat. Sc.*, 32, p. 1493, 1997.
11. J. W. Elmer, Joe Wong and Thorsten Ressler, "Spatially Resolved X-Ray Diffraction Mapping of Phase Transitions in the HAZ of Carbon-Manganese Steel Arc Welds," *Metall. and Mater. Trans. A*, 32A (5), pp. 1175-1187, 2001.
12. J. W. Elmer, T. A. Palmer, W. Zhang, B. Wood, and T. DebRoy, "Kinetic Modeling

of Phase Transformations Occurring in the HAZ of C-Mn Steel Welds Based on Direct Observations," *Acta Materialia*, V51, p3333, 2003.

13. S. S. Babu, J. W. Elmer, S. A. David and M. Quintana, "In-Situ Observations of Non-equilibrium Austenite Formation During Weld Solidification of a Fe-C-Al-Mn Low Alloy Steel," *Proceedings of the Royal Society: Mathematical, Physical and Engineering Sciences*, 458, pp 811-821, 2002.
14. J. W. Elmer, Joe Wong and Thorsten Ressler, "In-Situ Observations of Phase Transitions During Solidification and Cooling of Austenitic Stainless Steel Welds using Time-Resolved X-Ray Diffraction," *Scripta Materialia*, 43(8), pp. 751-757, 2000.
15. T. A. Palmer, J. W. Elmer, and Joe Wong, "In-Situ Observations of Ferrite/Austenite Transformations in Duplex Stainless Steel Weldments Using Synchrotron Radiation," *Science and Technology of Welding and Joining*, Vol. 7(3), pp 159-171, 2002.
16. *JADE, version 6.0*, Materials Data Inc., Livermore, California, 2001.
17. C. Barrett and T. Massalski: Structure of Metals, 3rd edition, Pergamon Press, 1982.
18. B. Sundman, B. Jansson and J. Andersson: Calphad-Computer Coupling of Phase Diagrams and Thermochemistry, V 9(2), p.153, 1985.
19. Babu S. S., Private communications, Oak Ridge National Laboratory, 2002.
20. W. Zhang, G. G. Roy, J. W. Elmer, and T. DebRoy, "Modeling of Heat Transfer and Fluid Flow during GTA Spot Welding of 1005 Steel," *Journal of Applied Physics*, V93(5), pp. 3022-3033, 1 Mar., 2003.
21. K. C. Mills : *Recommended values of thermophysical properties for selected commercial alloys*, ASM International, 2002.
22. C. J. Smithells, E. A. Brandes, and G. B. Brook : *Smithells Metal Reference Book*, 7th Edition, Butterworth-Heinemann Ltd., Oxford, United Kingdom, 1992.
23. J. W. Christian: The *Theory of Transformations in Metals and Alloys, 2nd Edition, Part I*, 1975, Oxford: Pergamon.
24. S. Malinov, Z. Guo, W. Sha and A. Wilson, "Differential Scanning Calorimetry Study and Computer Modeling of β α Phase Transforamation in a Ti-6Al-4V Alloy," *Metall. and Mater. Trans. A*, (32A), pp 879-887, 2002.

25. I. Katzov, S. Malinov, and W. Sha, “Finite Element Modeling of the Morphology of β to α Phase Transformations inTi-6Al-4VAlloy,” *Metall. and Mater. Trans. A*, (33), pp1027-1040, 2002.
26. M. B. Berkenpas et al., “A Critique of Activation Energies for Nucleation Growth and Overall Transformation Kinetics,” *Scripta Metall.*, V 20, pp 323-328, 1986.

Appendix

Effect of Shielding Gas on Surface Temperature during the TRXRD experiments

Helium gas was used to shield the area where the TRXRD measurements were being taken to eliminate the deposition of metallic particles. This cross jet of helium gas created an additional cooling effect on the surface of the weld. The cooling effect of the shielding gas was studied by considering heat transfer by forced convection, as the helium shielding gas impinges on the location where the x-ray beam is located. Table 1 summarizes the parameters and properties of the helium gas used in the experiments for the helium flow rate of $130 ft^3/hr$.

Table 1: Data used in the calculation of heat transfer coefficient by forced convection of the helium shielding gas.

Property of the shielding gas (He)	**Value**
T_{av}	1200 K
Density, ρ	0.1785 kg m^{-3}
Viscosity, μ	4.86×10^{-5} kg m^{-1} s^{-1} (4.86×10^{-4} g cm^{-1} s^{-1})
Specific heat, C_p	520 J kg^{-1} K^{-1}
Thermal conductivity, k	0.376 J m^{-2} s^{-1} K^{-1} (8.98×10^{-4} cal cm^{-2} s^{-1} K^{-1})
Gas flow rate, Q_g	1.02×10^{-3} m^3 s^{-1} (130 ft^3 hr^{-1})
Nozzle diameter, d	3.175×10^{-3} m (0.125 inch)
Gas flow velocity, u	129.1 m s^{-1}
Diameter of the workpiece, l	0.114 m
Re	1505
Pr	0.067

The effect of the shielding gas on the surface temperature was calculated by considering the convective heat transfer between the workpiece and surrounding gas, as given in the following equation [1]:

$$F_c = -h_c(T_s - T_g) \quad (1)$$

where F_c is the heat flux (J m^{-2} s^{-1}), T_s and T_g are surface and gas temperatures (K), respectively, and h_c is the heat transfer coefficient (J m^{-2} s^{-1} K^{-1}).

In order to use equation (1) to calculate the convective heat loss at the weld top surface, the knowledge of heat transfer coefficient (h_c) is required. In general, the value of h_c depends on the geometry of the system, the location along the surface, the fluid velocity, and the properties of the fluid. The heat transfer coefficient for a particular situation can be obtained either by direct measurement or from existing empirical or semi-empirical correlations. Some commonly used correlations are summarized in reference 2.

The shielding gas flowed in the tangential direction to the workpiece top surface. Thus, the following equation for a gas jet impinging on a solid surface [2] is used.

$$h_c = \frac{0.02\, k\, Re^{0.87}\, Pr^{0.33}}{l}$$

(2)

where l is the diameter of the workpiece (m), k is the thermal conductivity of shielding gas (J m^{-2} s^{-1} K^{-1}) at temperature T_{av}, which is the arithmetic average of T_l (liquidus temperature) and T_g, Re is the Reynolds number at the nozzle exit and Pr is the Prandtl number. The Reynolds number and Prandtl number are given by the following equations:

$$Re = \frac{\rho u d}{\mu} = \frac{4\rho Q_g}{\pi \mu d}$$

(3a)

$$Pr = \frac{C_p \mu}{k}$$

(3b)

where ρ, μ, and C_p are the density, viscosity and specific heat of the shielding gas, respectively, u is the velocity of the shielding gas at the nozzle exit and Q_g is the flow rate of the shielding gas. Using the data given in Table 1, the heat transfer coefficient is found to be 0.038 cal m^{-2} s^{-1} K^{-1}.

It should be noted that the heat transfer coefficient at the top surface may be a function of distance from the nozzle center. In other words, directly under the nozzle, the heat transfer coefficient should be a maximum, while far away from the nozzle the heat

transfer coefficient should be insignificant. Accurate determination of the spatial variation of heat transfer coefficient is difficult therefore, a constant heat transfer coefficient was assumed to be valid across the entire top surface of the bar [3].

References

[1] R. B. Bird, W. E. Stewart and E. N. Lightfoot: *Transport Phenomena*, John Wiley & Sons, New York, 1994, pg. 391.

[2] J. Szekely and N. J. Themelis: *Rate Phenomena in Process Metallurgy*, Wiley & Sons, Inc., New York, 1971, ch. 8.3.

[3] G. C. Huang, *J. Heat Transfer*, 85, 237 (1963).

Tables

Table 1: Summary of spot welding parameters used during the TRXRD experiments.

Weld	Average Current (Amp)	Voltage (V)	Arc On Time (s)	X-Ray location from weld center (mm)	Comments
1	100	19	20	4.5	fusion zone
2	100	19	17	5.0	fully transformed to β
3	100	19	17	5.5	partially transformed to β

Table 2: Chemical composition of the α and β phases in the base metal as measured by microprobe analysis. Seven points were averaged into each composition and the 1σ value is given as the estimated error.

	Al	V	Fe	Ti
Nominal Composition	6.2	4.0	0.17	89.6
β phase	2.92 ± 0.11	15.43 ± 0.86	1.32 ± 0.11	80.7 ± 0.70
α phase	6.73 ± 0.33	1.42 ±0.73	0.04 ± 0.02	91.2 ± 0.47

Table 3: Physical properties of Ti-6Al-4V used in the weld heat flow calculations.

Physical Property	Value
Liquidus Temperature, T_L, (K)	1928
Solidus temperature, T_S, (K)	1878
Density of liquid metal, ρ, (kg/m^3)	3.89×10^3
Effective viscosity of liquid, μ, (kg/m-s)	0.049
Thermal conductivity of liquid, k_L, (W/m-K)	32.5
Thermal conductivity of solid, k_S, (W/m-K)	8.3 to 24.2
Specific heat of solid, C_{PS}, (J/kg-K)	725
Specific heat of liquid, C_{PL}, (J/kg-K)	872
Temperature coefficient of surface tension, dγ/dT, (N/m-K)	-2.8×10^{-4}
Coefficient of thermal expansion, (K^{-1})	1.1×10^{-5}
Convective heat transfer coefficient top surface (W/m^2-K)	1.59×10^3

Table 4: Summary of the calculated JMA parameters for each of the weld locations, using two different assumptions about the dominant phase transformation mechanism. The underlined values of n and Q indicates the parameters that were held constant for the calculations.

Location	**n**	**ln(k_0)**	**Q (kJ/mol)**	**Average error**
X = 4.5 mm	*4*	8.2	144	0.0425
	6.3	6.4	*123.9*	0.0448
X = 5.0 mm	*4*	11.2	186	0.0640
	10.5	5.8	*123.9*	0.0646
X = 5.5 mm	*4*	12	188	0.0635
	8.8	6.4	*123.9*	0.0645
All Data	*4*	11.4	189	0.0547
	6.4	6.25	*123.9*	0.0647

Figures

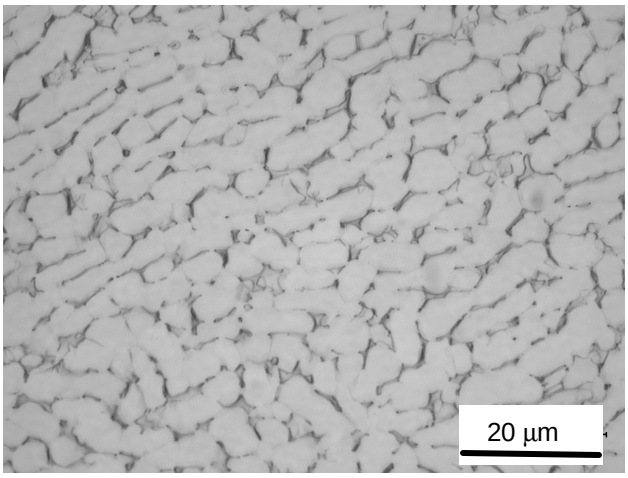

Figure 1: Base metal microstructure, showing intergranular β outlining the α grains.

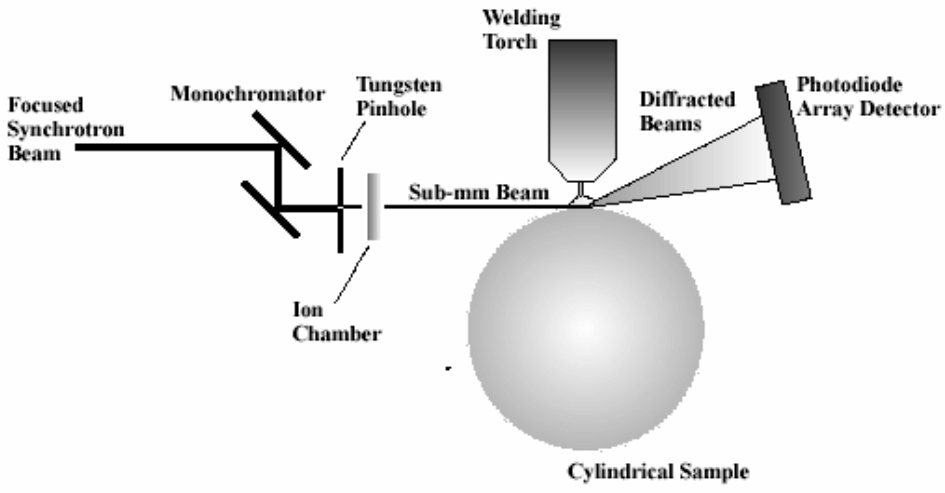

Figure 2: Schematic drawing of the TRXRD setup used for in-situ observations of phase transformations during welding.

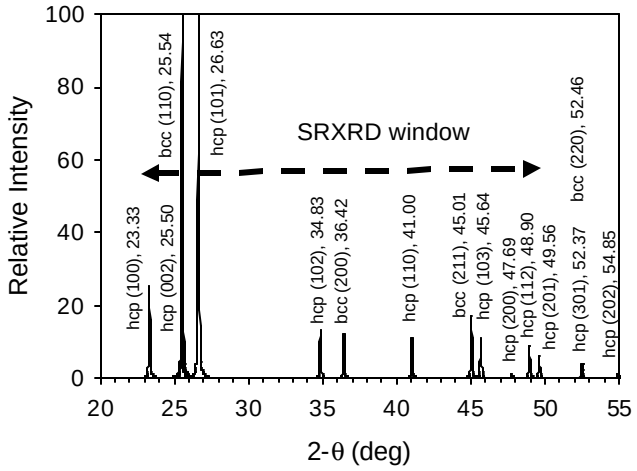

Figure 3: Calculated locations of the β-Ti (bcc) and α-Ti (hcp) peaks that can appear from 20° to 55° of 2θ at 12.0 keV. The 2θ window of the X-ray detector is indicated by the horizontal dashed line.

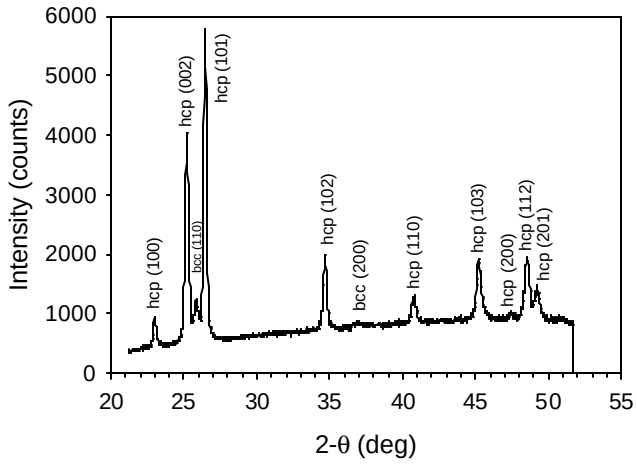

Figure 4: Initial SRXRD diffraction pattern taken on the Ti-6Al-4V bar prior to welding. This pattern was acquired in 10s, the same amount of time as used during the welding experiments.

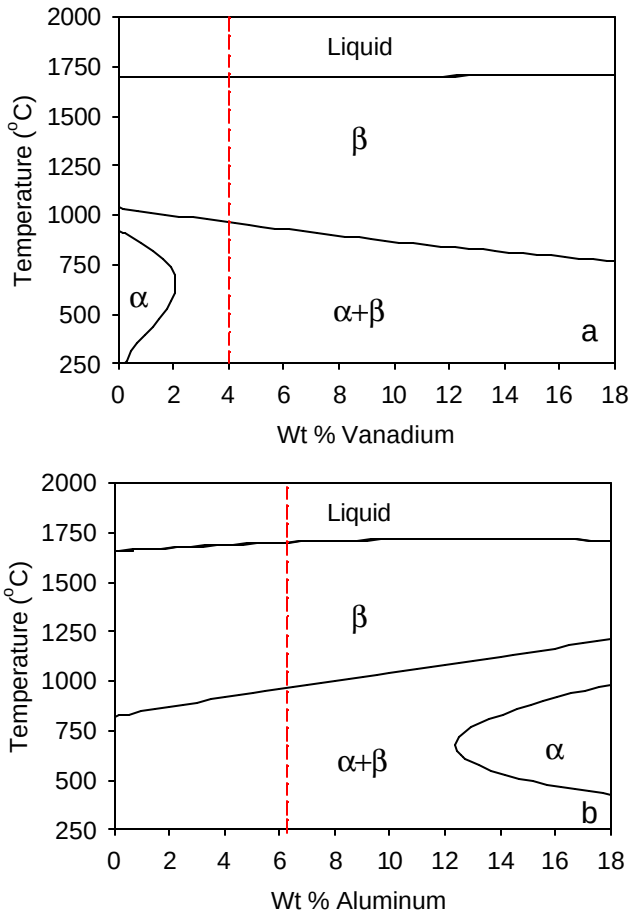

Figure 5: Binary-alloy phase equilibrium calculated by thermocalc showing the influence of : a) the V content on the α and β phase equilibrium, and b) the Al content on the α and β phase equilibrium. The vertical lines indicate the nominal V and Al contents of the alloy.

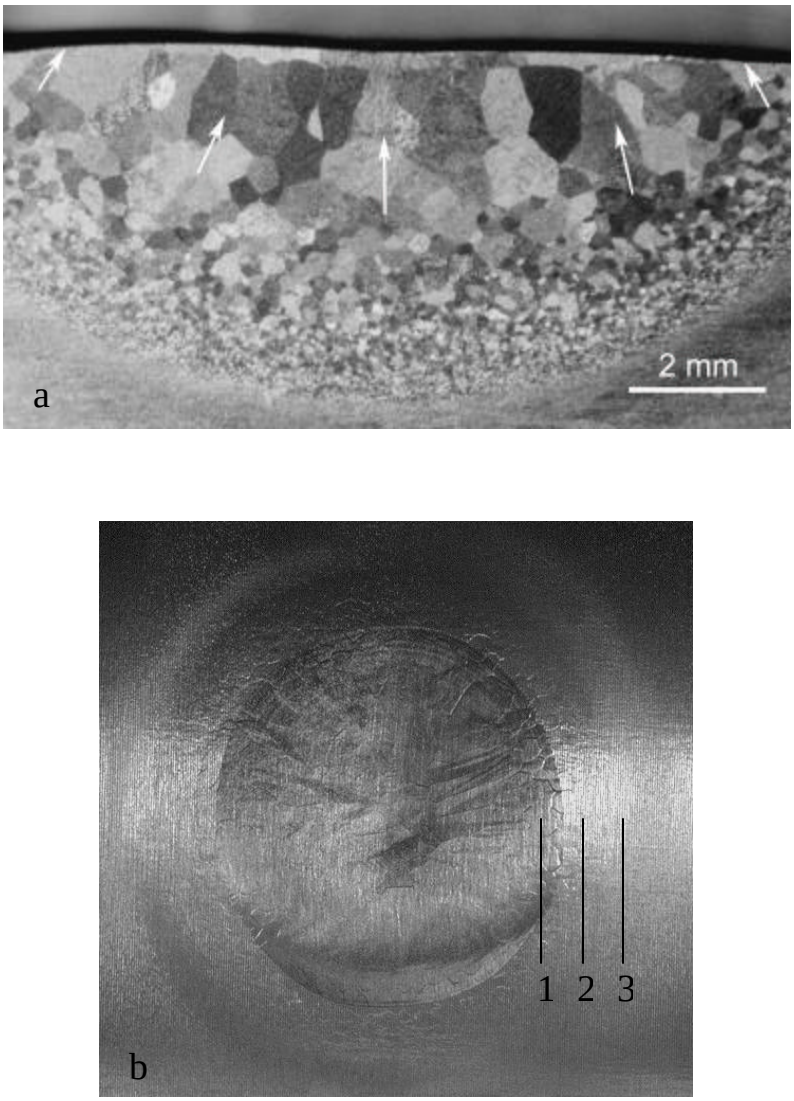

Figure 6 : a) Metallographic cross section of the weld. The white arrows point to the fusion zone boundary. b) Macrophotograph of the top surface of one of the welds indicating the relative positions of the three x-ray locations with respect to the fusion line.

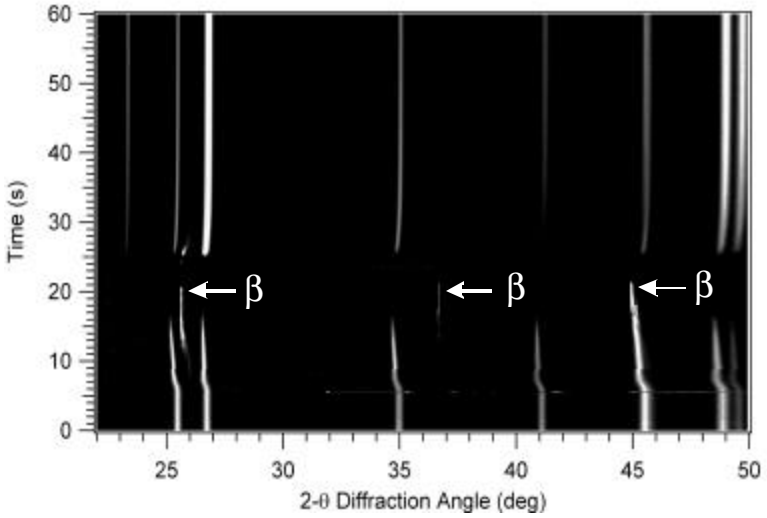

Figure 7: Overview of the TRXRD diffraction patterns for weld 1. The arc was initiated at t=5.8s, complete melting occurred at t=23.8s and solidification initiated at t=25.1s. Complete transformation to β occurs at t=17.8s, leaving only the three β peaks (indicated by arrows) present just before melting.

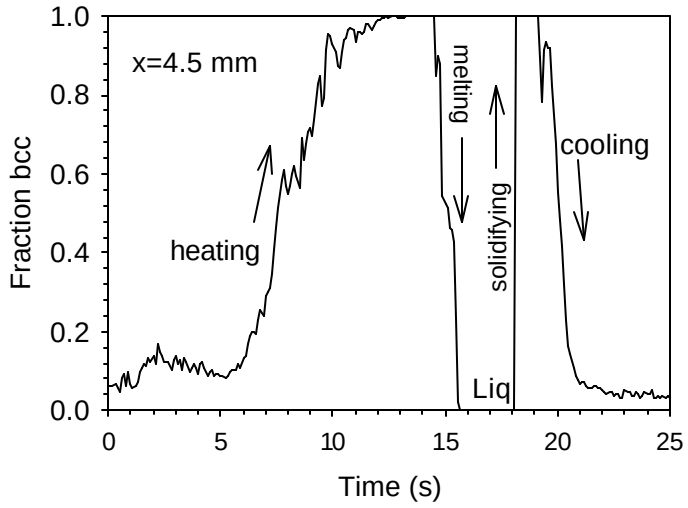

Figure 8: Relative area fractions of the β phase in weld 1, where the beam was positioned 4.5 mm from the center of the weld. Melting and solidification was observed at this FZ location.

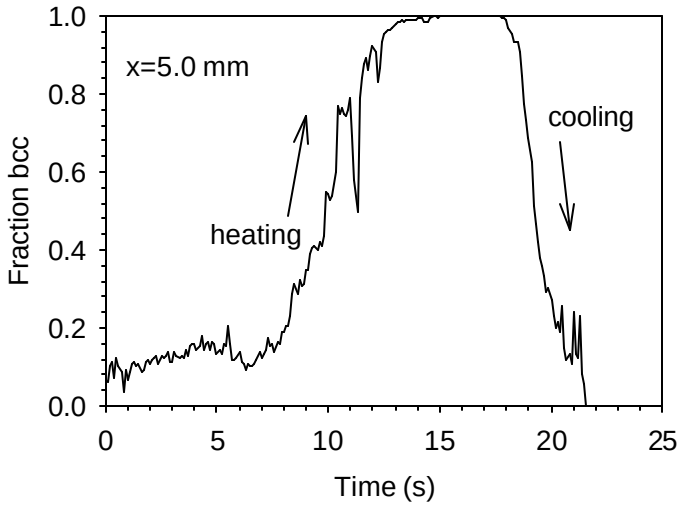

Figure 9: Relative area fraction of the β phase in weld 2, where the beam was positioned 5.0 mm from the center of the weld. At this location, the HAZ underwent a complete transformation to the β phase.

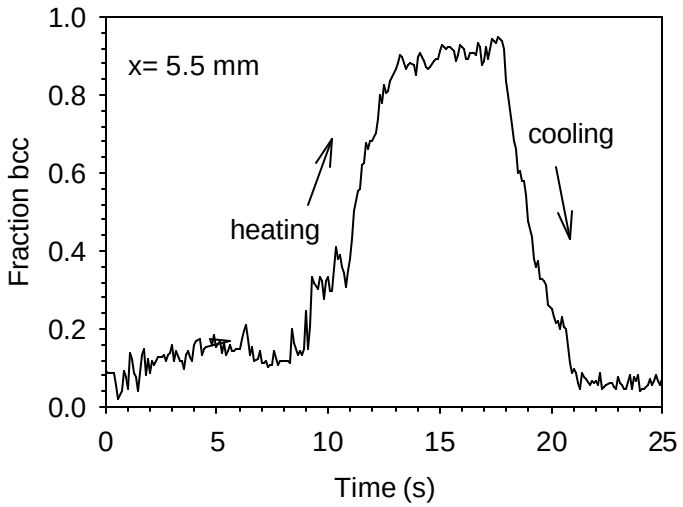

Figure 10: Relative area fractions of the β phase in weld 3, where the beam was positioned 5.5 mm from the center of the weld. At this HAZ location only partial transformation to β was observed.

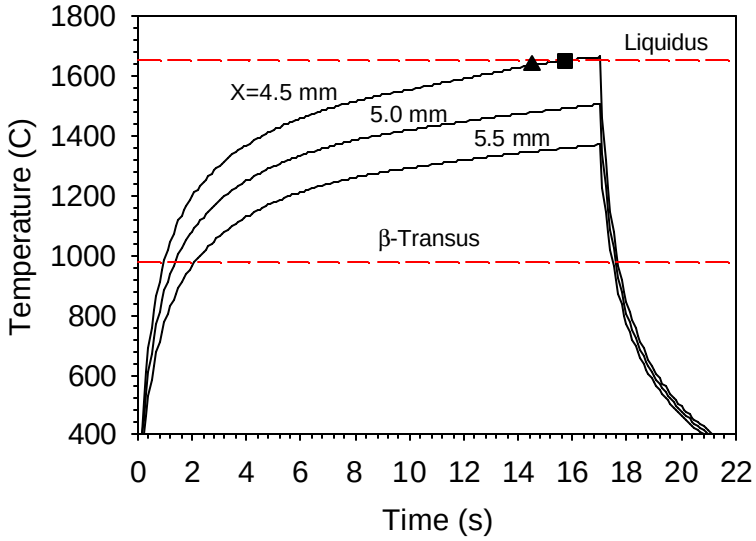

Figure 11: Results of the coupled thermal-fluids model showing the calculated weld thermal cycles at the three x-ray locations. The triangle marks the TRXRD time where melting was observed to begin, and the square where melting was observed to be complete.

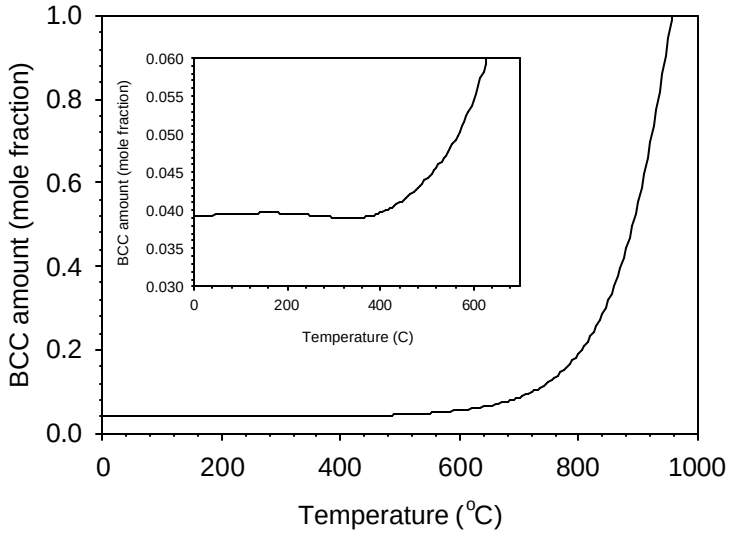

Figure 12: Thermocalc results plotting the equilibrium fraction β (bcc) versus temperature. The inset plot shows the low temperature behavior and indicates a slight dip in β around 400 °C.

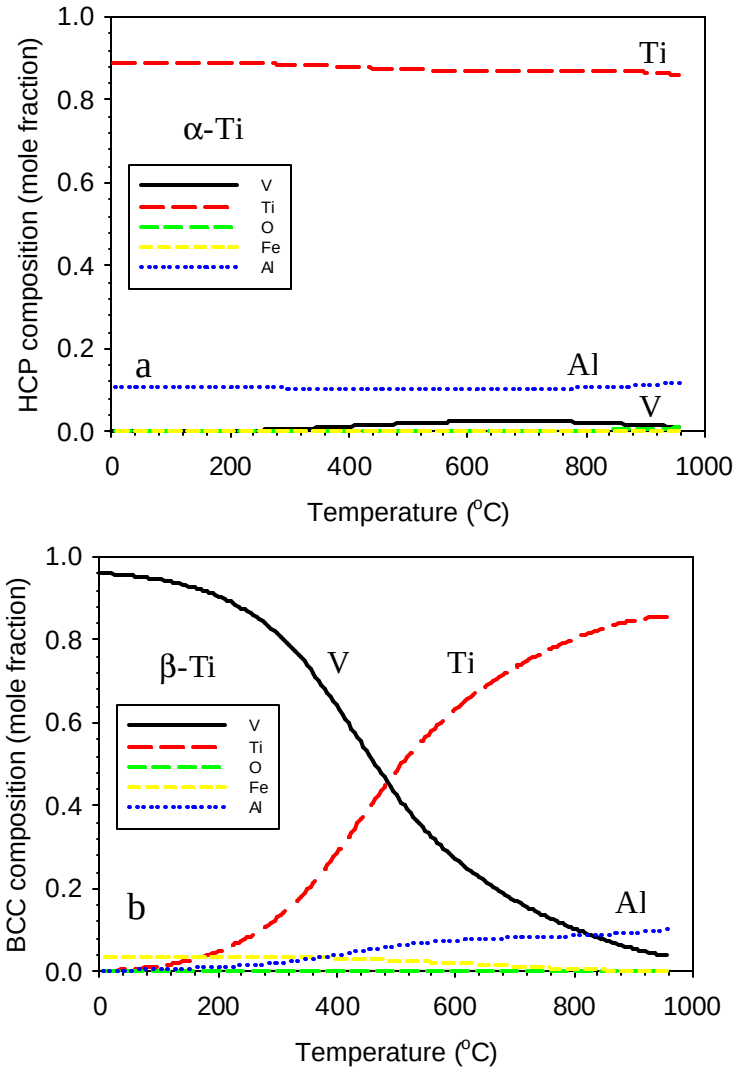

Figure 13: Thermocalc results showing the individual compositions of a) the α phase and b) the β phase as a function of temperature.

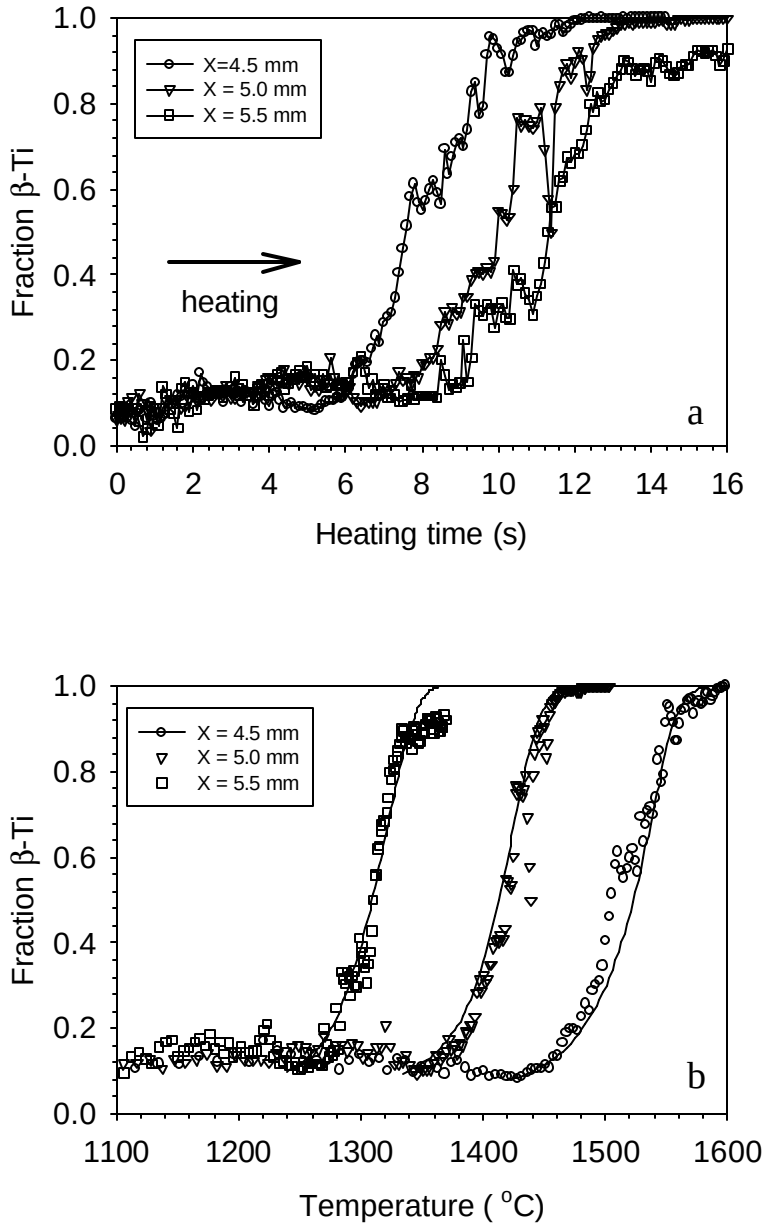

Figure 14: TRXRD results showing fraction β during the heating cycle of the weld plotted versus a) weld time after arc is on, and b) weld temperature, where the solid lines mark the JMA fit to the data using a fixed value of n=4.0.

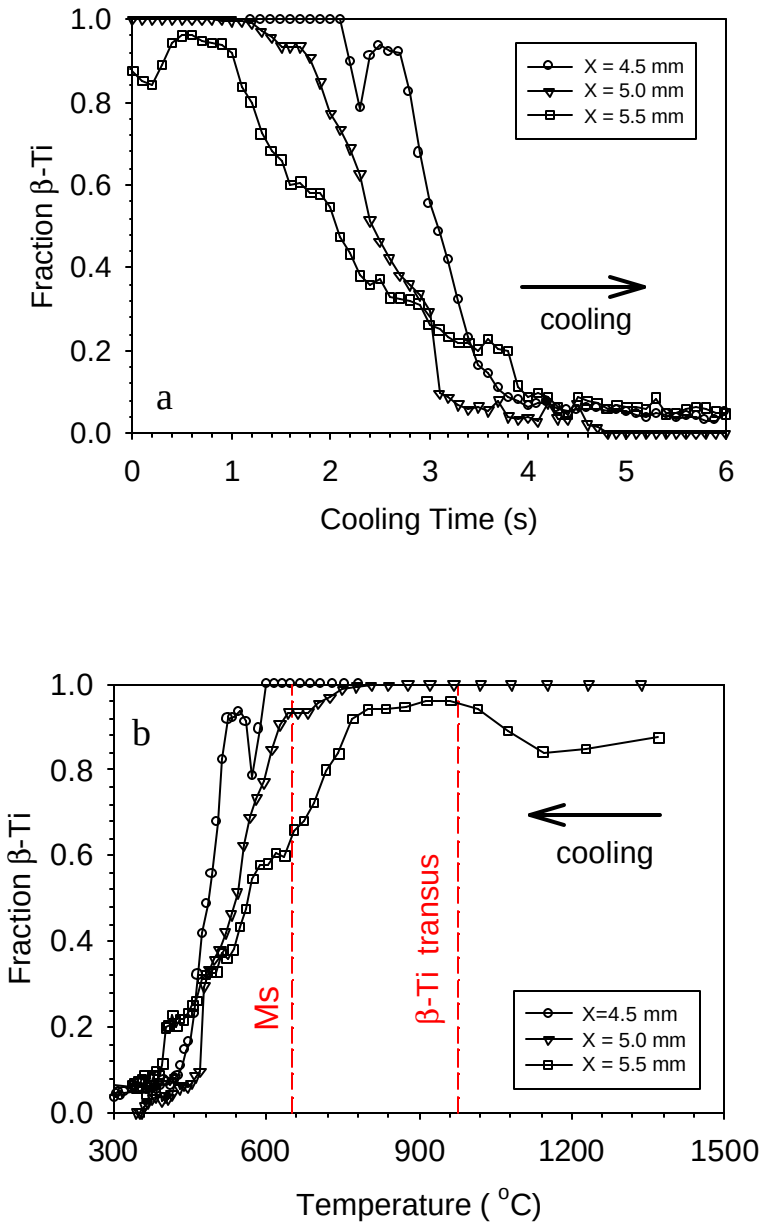

Figure 15: TRXRD results showing fraction β during the cooling cycle of the weld plotted versus a) weld time after arc is off and b) weld temperature. The vertical dashed lines mark the calculated α/β transus, and the approximate Ms temperature for this alloy.

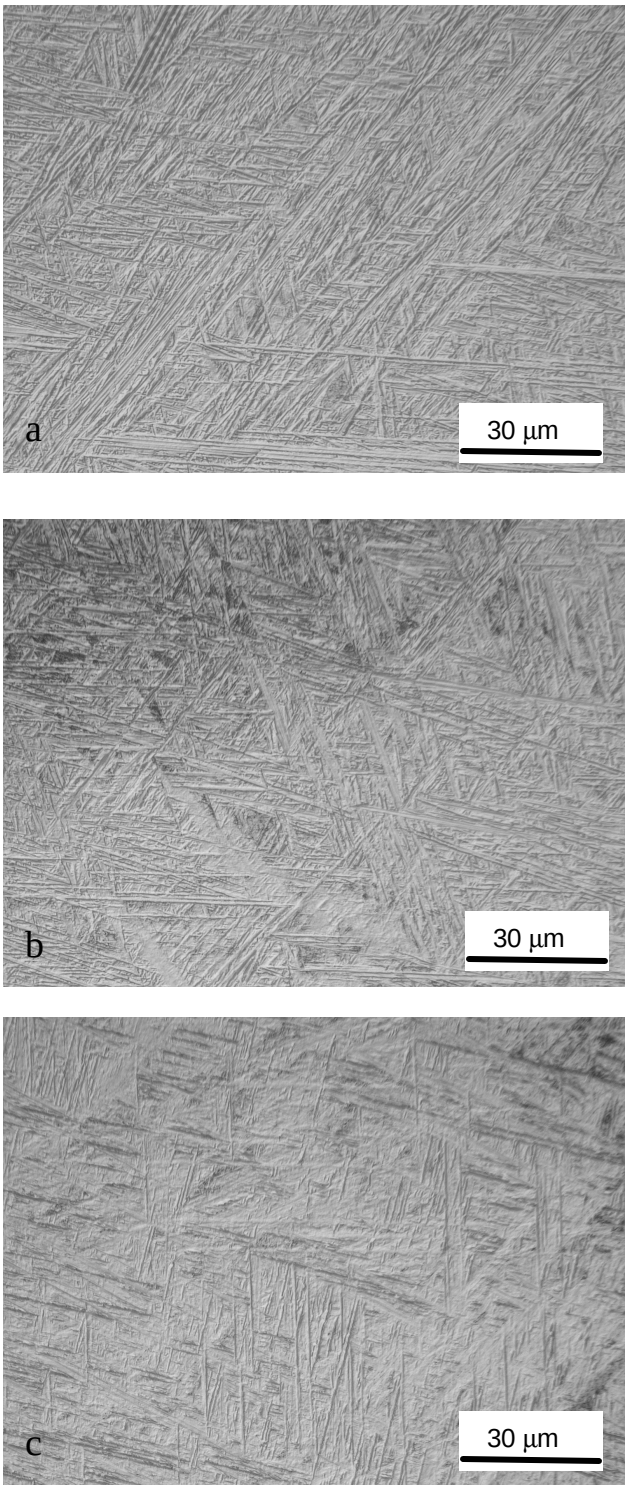

Figure 16: High magnification micrographs taken of the weld microstructure at each of the three locations. a) weld 1 fusion zone, 4.5 mm from weld center, b) weld 2 HAZ, 5.0 mm from weld center, and c) weld 3 HAZ, 5.5 mm from weld center.